TU Delft

Delft University of Technology

Exploring the negative thermal expansion and magnetocaloric effect in Fe_2(Hf,Ti) Laves phase materials

Shen, Qi; Batashev, Ivan; Zhang, Fengqi; Ojiyed, Hamutu; Dugulan, Iulian; van Dijk, Niels; Brück, Ekkes

DOI
10.1016/j.actamat.2023.119149

Publication date
2023

Document Version
Final published version

Published in
Acta Materialia

Citation (APA)
Shen, Q., Batashev, I., Zhang, F., Ojiyed, H., Dugulan, I., van Dijk, N., & Brück, E. (2023). Exploring the negative thermal expansion and magnetocaloric effect in Fe_2(Hf,Ti) Laves phase materials. *Acta Materialia*, *257*, Article 119149. https://doi.org/10.1016/j.actamat.2023.119149

Important note
To cite this publication, please use the final published version (if applicable).
Please check the document version above.

Copyright
Other than for strictly personal use, it is not permitted to download, forward or distribute the text or part of it, without the consent of the author(s) and/or copyright holder(s), unless the work is under an open content license such as Creative Commons.

Takedown policy
Please contact us and provide details if you believe this document breaches copyrights.
We will remove access to the work immediately and investigate your claim.

This work is downloaded from Delft University of Technology.
For technical reasons the number of authors shown on this cover page is limited to a maximum of 10.

Acta Materialia 257 (2023) 119149

Contents lists available at ScienceDirect

Acta Materialia

journal homepage: www.elsevier.com/locate/actamat

Exploring the negative thermal expansion and magnetocaloric effect in $Fe_2(Hf,Ti)$ Laves phase materials

Qi Shen [a,*], Ivan Batashev [b], Fengqi Zhang [a], Hamutu Ojiyed [a], Iulian Dugulan [a], Niels van Dijk [a], Ekkes Brück [a]

[a] Fundamental Aspects of Materials and Energy, Faculty of Applied Sciences, Delft University of Technology, Mekelweg 15, 2629 JB Delft, the Netherlands
[b] Institute for Molecules and Material, Radboud University, Heyendaalseweg 135, 6525 AJ Nijmegen, the Netherlands

ARTICLE INFO

Keywords:
Negative thermal expansion
Magnetocaloric effect
Second-order phase transition
Neutron diffraction

ABSTRACT

The transition-metal based Laves phase materials represent an extended family of alloys with rich and fascinating physical properties. In this work, we have investigated the negative thermal expansion and magnetocaloric effect in arc-melted and melt-spun $Fe_2Hf_{1-x}Ti_x$ ($x = 0.15, 0.27, 0.30, 0.33, 0.36, 0.40$) alloys. For $x = 0.30$–0.40, two hexagonal phases with different compositions share the same $P6_3/mmc$ lattice symmetry, but have slightly different lattice parameters. The saturation magnetization and Curie temperature both follow a decreasing trend with the average unit-cell volume. For $Fe_2Hf_{0.6}Ti_{0.4}$ melt spinning improves the saturation magnetization from 48.7 to 59.6 Am^2/kg and the magnetic entropy change from 0.46 to 0.54 J/kgK at a magnetic field change of 2 T. These enhanced values are attributed to an improved homogeneity caused by a suppression of phase segregation during rapid solidification. We have utilized neutron powder diffraction and Mössbauer spectroscopy to illustrate the correlation between the magnetic order and the negative thermal expansion in single-phase $Fe_2Hf_{0.85}Ti_{0.15}$. The magnetic moments of Fe align below 400 K in the *a-b* plane and a moment change for the Fe atoms is responsible for the large volumetric coefficient of thermal expansion of $-25 \times 10^{-6}\ K^{-1}$ over a wide temperature range of 300–400 K.

1. Introduction

The magnetocaloric effect (MCE) is the caloric response of the lattice on the application or removal of a magnetic field and can be characterized by the magnetic entropy change and the adiabatic temperature change [1,2]. In terms of the energy efficiency and environmental safety of MCE-based magnetic refrigeration, the exploration of new MCE materials and the understanding of the mechanism controlling the magnetic phase transition have attracted much attention in recent decades [3,4]. Many magnetocaloric materials undergoing a magnetostructural or a magnetoelastic transition have been studied, such as Mn-Fe-P-Si [5,6], $La(Fe,Si)_{13}$ [7,8], Ni-Mn-based Heusler alloys [9,10], MnCoGe [11], $Fe_2(Hf,Ta)$ [12–14] and Mn_2Sb [15–17]. Due to the strong spin-lattice coupling, some of the magnetocaloric materials, such as La-Fe-Si-Co [18], MnCoGe [19], and Fe-based Laves phase materials [20,21], are also considered as potential candidates for negative thermal expansion (NTE) materials, which are in high demand in modern industry for the adjustment of the thermal expansion in materials [22,23]. Among them magnetic Fe-based Laves phase materials combine a spontaneous magnetization with a magnetoelastic lattice volume contribution based on two different Fe atomic sites, which combine the advantages of a high thermal conductivity and good mechanical properties for NTE and magnetocaloric applications [20,14].

MCE materials with a large magnetic entropy change generally show a large change in magnetic moment. It is well known that itinerant electron systems with a large magnetic moment have a larger unit-cell volume. Therefore, a steep change in magnetization for itinerant electron systems is generally linked to a steep change in volume, except for magnetic materials that rather change *c/a* ratios, which may yet occur without volume change. An interesting example is the $Fe_2(Hf,Ta)$ Laves phase compound, which shows a sharp magnetization jump at the ferromagnetic-to-antiferromagnetic phase transition, accompanied by a negative thermal expansion effect [24]. This sharp transition is due to a frustration effect, in which the magnetic moment of the Fe atom at the

* Corresponding author at: Fundamental Aspects of Materials and Energy, Faculty of Applied Sciences, Delft University of Technology, Mekelweg 15, 2629 JB Delft, The Netherlands.
E-mail address: q.shen@tudelft.nl (Q. Shen).

https://doi.org/10.1016/j.actamat.2023.119149
Received 3 February 2023; Received in revised form 5 July 2023; Accepted 10 July 2023
Available online 11 July 2023
1359-6454/© 2023 The Author(s). Published by Elsevier Ltd on behalf of Acta Materialia Inc. This is an open access article under the CC BY license (http://creativecommons.org/licenses/by/4.0/).

2*a* site of the hexagonal $P6_3/mmc$ structure (space group 194) disappears below the transition temperature [25]. This leads to a large adiabatic temperature change of about 3.4 K in the presence of a relatively small change in applied magnetic field of 1.5 T [14]. The tuneable transition temperature, large adiabatic temperature change and small thermal hysteresis make these compounds attractive for magnetocaloric applications [13,14]. On the other hand, the linear NTE coefficient of $-16.3 \times 10^{-6}\,K^{-1}$ over a broad temperature window of 105 K (222–327 K) is attributed to the asynchronous ferromagnetic ordering of the Fe moments at the 6*h* and 2*a* sites revealed by Electron Spin Resonance [20]. A similar magnetoelastic transition has also been observed in Fe-based Fe_2(Sc,Ti) [21], Fe_2(Hf,Ti) [26] and Fe_2(Hf,Nb) [27] Laves phase materials. So far however, there have only been a limited number of systematic reports on the mechanism responsible for the magnetoelastic coupling in Fe-based Laves phase materials.

In this work, Mössbauer spectroscopy, neutron powder diffraction and DFT calculations are employed to investigate the correlation between the negative thermal expansion and the magnetic behaviour in Fe_2(Hf,Ti) compounds. In addition, we propose a materials fabrication method to enhance the magnetocaloric effect in Fe_2(Hf,Ti) Laves phase materials by supressing phase segregation using melt spinning technique.

2. Experimental methods

Polycrystalline $Fe_2Hf_{1-x}Ti_x$ (x = 0.15, 0.27, 0.30, 0.33, 0.36, 0.40) compounds were prepared from high-purity elements (Fe 99.98%, Hf 99.95%, Ti 99.99%) by arc melting. Samples with a total mass of 5 g were melted four or five times, and the button-shaped alloys were flipped over after each melting. Four different heat treatments were tried for $x = 0.36$: (a) annealing at 1173 K for 24 h and quenching; (b) annealing at 1273 K for 134 h and quenching; (c) annealing at 1323 K for 24 h and quenching; (d) annealing at 1373 K for 24 h and quenching. All these heat treatments resulted in comparable lattice parameters, saturation magnetizations and transition temperatures (see Fig. S1 in Supplementary Material). Accordingly, only as-cast samples are reported for most compositions (with some exceptions noted in the manuscript). For $Fe_2Hf_{1-x}Ti_x$ (x = 0.36, 0.40) compounds, the melt-spinning technique is used to improve homogeneity. The crucible of melt-spinning device is a commercial quartz tube with a melting point of 1883 K. The melting point of $Fe_2Hf_{1-x}Ti_x$ is estimated to be about 1673 K. The melt-spun ribbons were produced under argon atmosphere at different surface speeds of the copper wheel. By comparing the melt-spun ribbons with different heat treatments (see Fig. S2 in Supplementary Material), those without a heat treatment are characterized for the discussion.

X-ray diffraction (XRD) data were collected with a Panalytical X-Pert PRO using Cu-K_α radiation and an Anton Paar TTK 450 temperature chamber. The lattice structure was analysed by Rietveld refinement using Fullprof [28]. The magnetic properties at low temperature (4–370 K) were measured using a superconducting quantum interference device (SQUID) magnetometer model MPMS-XL, equipped with the reciprocating sample option. Magnetisation measurements at high-temperature (315–650 K) were carried out using a vibrating sample magnetometer (VSM) model LakeShore 7307 equipped with a high-temperature furnace (model 73,034). The ferromagnetic transition temperature T_C is determined from the minimum in the temperature derivative of the magnetization as a function of temperature at an applied magnetic field of 1 T. The magnetic entropy change was calculated from the *M-T* curves obtained at different magnetic fields using the Maxwell relations. Differential scanning calorimetry (DSC) measurements were performed in a commercial TA-Q2000 DSC calorimeter (at a sweep rate of 10 K/min). The microstructure was analysed by scanning electron microscopy (SEM) using a FEI Quanta FEG 450 equipped with energy dispersive X-ray spectroscopy (EDS). Transmission ^{57}Fe Mössbauer spectra were collected at different temperatures in the range from 4.2 to 300 K with conventional constant-acceleration or sinusoidal velocity spectrometers using a ^{57}Co(Rh) source. The velocity calibration was performed using an α-Fe foil at room temperature. The source and the absorbing samples were kept at the same temperature during the cryogenic measurements. The Mössbauer spectra were fitted using the Mosswinn 4.0 program [29]. Powder neutron diffraction (ND) data at different temperatures were collected at a wavelength of 1.6672 Å using the ND apparatus PEARL [30] at the research reactor of Delft University of Technology. The crystal structures and the atomic occupancies were refined using the Rietveld refinement method implemented in the Fullprof software package [31–33].

Density functional theory (DFT) modelling was performed with the Vienna ab initio simulation package (VASP) [34,35]. Exchange interactions were taken into account by using the generalized gradient approximation (GGA) by Perdew, Burke, and Ernzerhof (PBE) [36]. For all calculations, the projector augmented-wave (PAW) [37,38] pseudopotentials were used with the valence electron configuration 5*p*5*d*6*s* for Hf, 3*s*3*p*3*d*4*s* for Ti and 3*d*4*s* for Fe. All calculations were performed for a 1×1×2 supercell. The structural degrees of freedom were fully relaxed on a gamma centred *k*-grid of 11×11×3. The *k*-space integrations were performed using the second order Methfessel-Paxton method [39] with a smearing width of 0.05 eV. The lattice parameters and atomic positions were optimized with the criteria that the atomic force is weaker than 0.1 meV/Å and an energy convergence of 1 μeV. The kinetic energy cutoff was set at 400 eV.

3. Results and discussion

Fig. 1(a) shows the XRD patterns for arc-melted $Fe_2Hf_{1-x}Ti_x$ (x = 0.15, 0.27, 0.30, 0.33, 0.36, 0.40), denoted as TiX alloys (where X corresponds to the Ti fraction x). With increasing Ti substitution, the peaks become broader, which is seen in the enlarged region in Fig. 1(b) and the increased full width at half-maximum (FWHM) of (110) and (003) peaks in Fig. 2(a). All samples crystalize in the hexagonal $MgZn_2$-type structure with $P6_3/mmc$ symmetry (space group 194), where the Fe atoms occupy the 2*a* and 6*h* sites and the Hf/Ti atoms occupy the 4*f* site. According to the Rietveld refinement results in Fig. 1(c) the patterns for the Ti0.15 and Ti0.27 samples can be fitted best as single-phase hexagonal. The other four samples, for example the Ti0.36 sample in Fig. 1 (d) can be fitted best by a two-phase model. These two phases share the same space group 194, but with slightly different lattice parameters. The refined lattice parameters are given in Fig. 2(d-f). The fraction of the Ti-rich phase P1 increases with increasing Ti content. The average unit-cell volume, based on the fraction of the two phases P1 and P2, decreases linearly with Ti content.

To confirm the presence of phase segregation, the backscattered electron SEM images of the Ti0.36 sample are shown in Fig. 2(b). The dark region refers to the Ti-rich phase, corresponding to P1. The chemical compositions of the matrix and Ti-rich phase are determined by EDS and are found to be $Fe_{65.9}Hf_{25.5}Ti_{8.6}$ and $Fe_{66.3}Hf_{19.7}Ti_{14.0}$, respectively. It is found that this phase segregation is difficult to avoid by different heat treatments (see Fig. S1 in Supplementary Material). It is worthwhile to note that in $Hf_{0.6}Ti_{0.4}Fe_2$ a similar XRD peak broadening is attributed to a phase coexistence of AFM and FM states [26], where the homogeneity is supported by SEM mapping at the scale of 100 μm. A variation in chemical composition at a smaller length scale or in other areas of the samples cannot be excluded [40]. From the insert picture in Fig. 2(c), the annealed Ti0.36 sample (annealed at 1273 K for 134 hours) exhibits significant compositional fluctuations, as indicated from the line-scan profile across the Ti-rich boundaries. The chemical composition of the matrix and the Ti-rich phases are $Fe_{65.4}Hf_{27.0}Ti_{7.6}$ and $Fe_{65.3}Hf_{18.3}Ti_{16.3}$, respectively.

The *M-T* curves in Fig. 3(a) show that the magnetization decreases continuously with increasing temperature for the arc-melted Ti0.15 sample. With decreasing temperature it follows the same trajectory without any thermal hysteresis, which suggests a second-order phase transition from the ferromagnetic to the paramagnetic phase. Fig. 3(b)

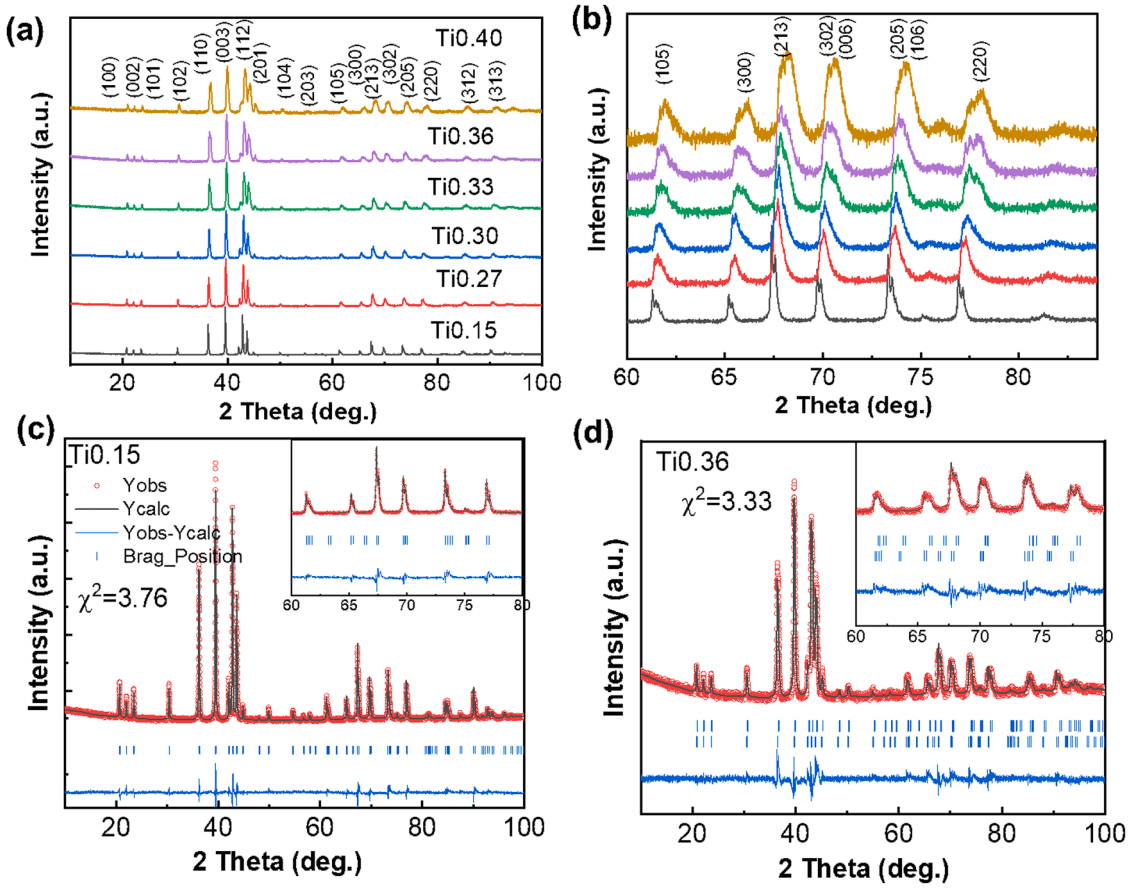

Fig. 1. (a) XRD patterns of arc-melted $Fe_2Hf_{1-x}Ti_x$(x = 0.15, 0.27, 0.30, 0.33, 0.36). (b) Zoomed-in region between 60 and 90° from (a). (c, d) Rietveld refinement results of the arc-melted Ti0.15 and Ti0.36 samples with the zoomed-in region of 60–80° in the inset graphs.

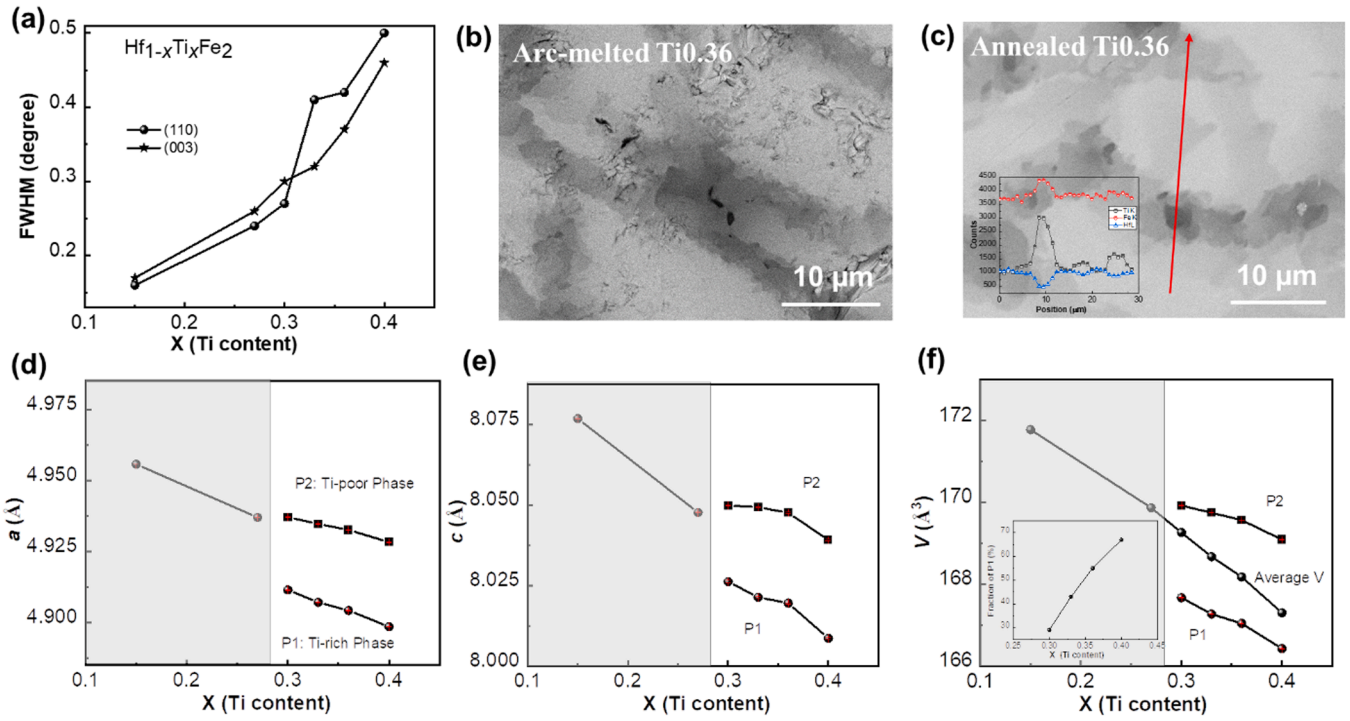

Fig. 2. (a) Full width at half-maximum (FWHM) of (110) and (003) peaks for arc-melted $Fe_2Hf_{1-x}Ti_x$ (x = 0.15, 0.27, 0.30, 0.33, 0.36, 0.40). Backscattered electron SEM images of (b) arc-melted Ti0.36 sample without any heat treatment and (c) arc-melted Ti0.36 sample annealed at 1273 K for 134 h. (d, e, f) Ti-content dependence of the lattice parameters a and c and the unit-cell volume V. The inset in (f) is the fraction of the Ti-rich P1 phase as a function of the Ti content.

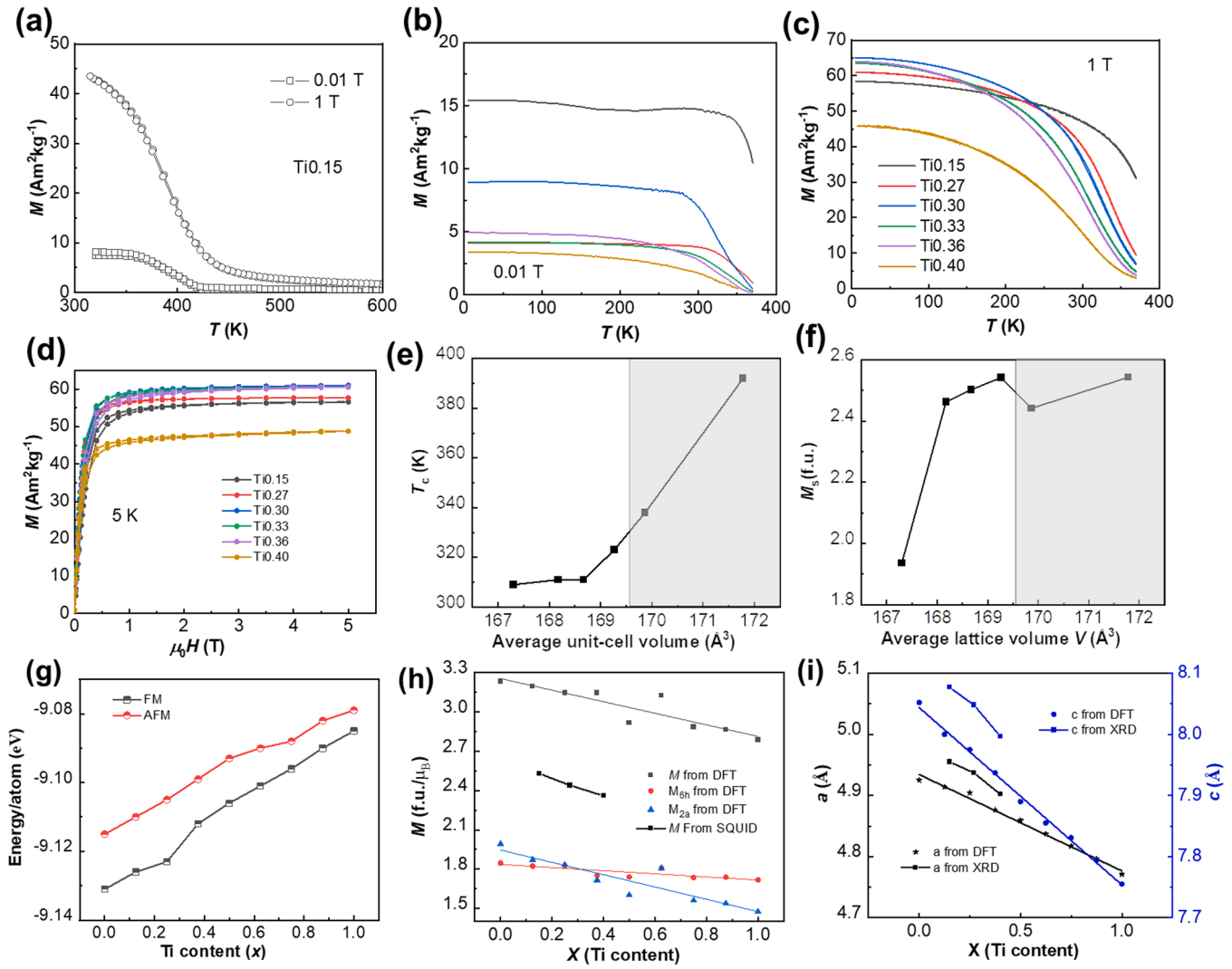

Fig. 3. (a) *M-T* curves for the Ti0.15 sample. (b) *M-T* curves of $Fe_2Hf_{1-x}Ti_x$ upon heating in a magnetic field of 0.01 T and (c) *M-T* curves of $Fe_2Hf_{1-x}Ti_x$ upon heating in a magnetic field of 1 T. (d) *M-H* curves for $Fe_2Hf_{1-x}Ti_x$ at a temperature of 5 K. (e) T_C as a function of the average unit-cell volume of $Fe_2Hf_{1-x}Ti_x$. (f) M_s as a function of average unit-cell volume of $Fe_2Hf_{1-x}Ti_x$. DFT calculation results for the $Fe_2Hf_{1-x}Ti_x$ alloys with: (g) formation energy for the ferromagnetic (FM) and antiferromagnetic (AFM) phase, (h) calculated magnetic moment, and (i) calculated lattice parameters *a* and *c* as a function of the Ti content. For the single-phase samples (arc-melted Ti0.15, Ti0.27 and melt-spun Ti0.40), the experimental magnetic moment and lattice parameters are also given for comparison in (h) and (i), respectively.

and 3(c) show the *M-T* curves for $Fe_2Hf_{1-x}Ti_x$ ($x = 0.15, 0.27, 0.30, 0.33, 0.36, 0.40$) compounds in a magnetic field of 0.01 and 1 T, respectively. T_C initially decreases linearly with the average unit-cell volume and then stabilizes around 310 K, as seen in Fig. 3(e). Substitution of Hf by Ti decreases the atomic spacing of the Fe atoms and leads to a suppression of the FM order, so that T_C can be tuned between 310 and 390 K by changing the Ti content. A series of *M-H* curves was measured at 5 K, as shown in Fig. 4(d). All samples reach a magnetic saturation at the highest field of 5 T. A significant decrease in saturation magnetization is observed for the Ti0.40 sample due to the lower saturation magnetization from the dominant Ti-rich phase (67%). We employed spin-polarized DFT calculations for the formation energy, lattice parameters and magnetic moment, as shown in Fig. 3(g-i). Two magnetic configurations: (*i*) ferromagnetic (FM) structure, with the Fe moments at the 2*a* and 6*h* sites orientated in the *a-b* plane and (*ii*) antiferromagnetic (AFM) structure, with at the 6*h* site ferromagnetically aligned intralayer Fe magnetic moments and antiferromagnetically aligned interlayer Fe magnetic moments with unordered Fe magnetic moments at the 2*a* site [13] are considered in our DFT calculations (see Fig. S3 in Supplementary Material). Comparing the formation energy of the two magnetic configurations, the FM structure is the more favourable one. As the Ti content increases, the energy difference decreases (in Fe_2Ti the energy difference is merely 6 meV/atom) because the FM is destabilized by the decrease in lattice parameters due to the smaller atomic size of Ti compared to Hf [41]. The total magnetic moment also decreases with increasing Ti content. It is worth noting that the magnetic moment of Fe at the 2*a* site is more sensitive to the Ti content than that of Fe at the 6*h* site. This stronger instability of the Fe magnetic moment at 2*a* site is also reported in $Ti_{0.70}Sc_{0.30}Fe_2$, as observed by neutron diffraction [42]. The lattice parameter decreases linearly with increasing Ti content. For single-phase samples, the magnitude of the calculated lattice parameter and magnetic moment are in agreement with the values obtained from XRD and SQUID, as shown in Fig. 3(h) and Fig. 3(i). The spin-polarized density of states (DOS) for $Fe_2Hf_{1-x}Ti_x$ ($x = 0.125, 0.25, 0.375$) is shown in Fig. S4. For an increasing Ti substitution the lattice shrinks and the Fermi energy moves towards a lower energy, resulting in a lower magnetization and a lower T_C. The substitution of the Ti atom for the Hf atom brings a peak in the DOS close to the Fermi level, which results in a significant impact on the magnetic interactions.

Phase segregation has also been reported in other Fe-based Laves

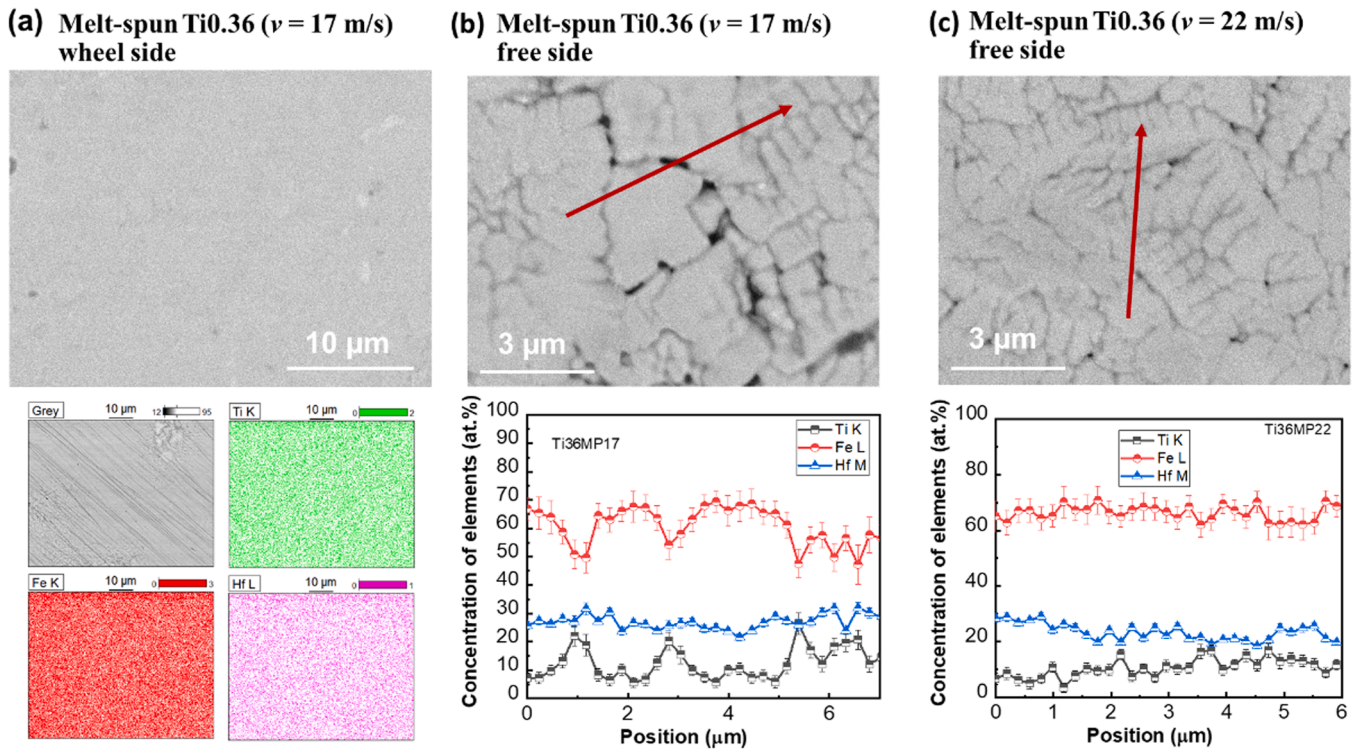

Fig. 4. (a) Backscattered electron SEM images and mapping for the melt-spun Ti0.36 (17 m/s) sample. Backscattered electron SEM images and line-scanning profile along the red line (b) for the melt-spun Ti0.36 (17 m/s) sample and (c) for the melt-spun Ti0.36 (22 m/s) sample.

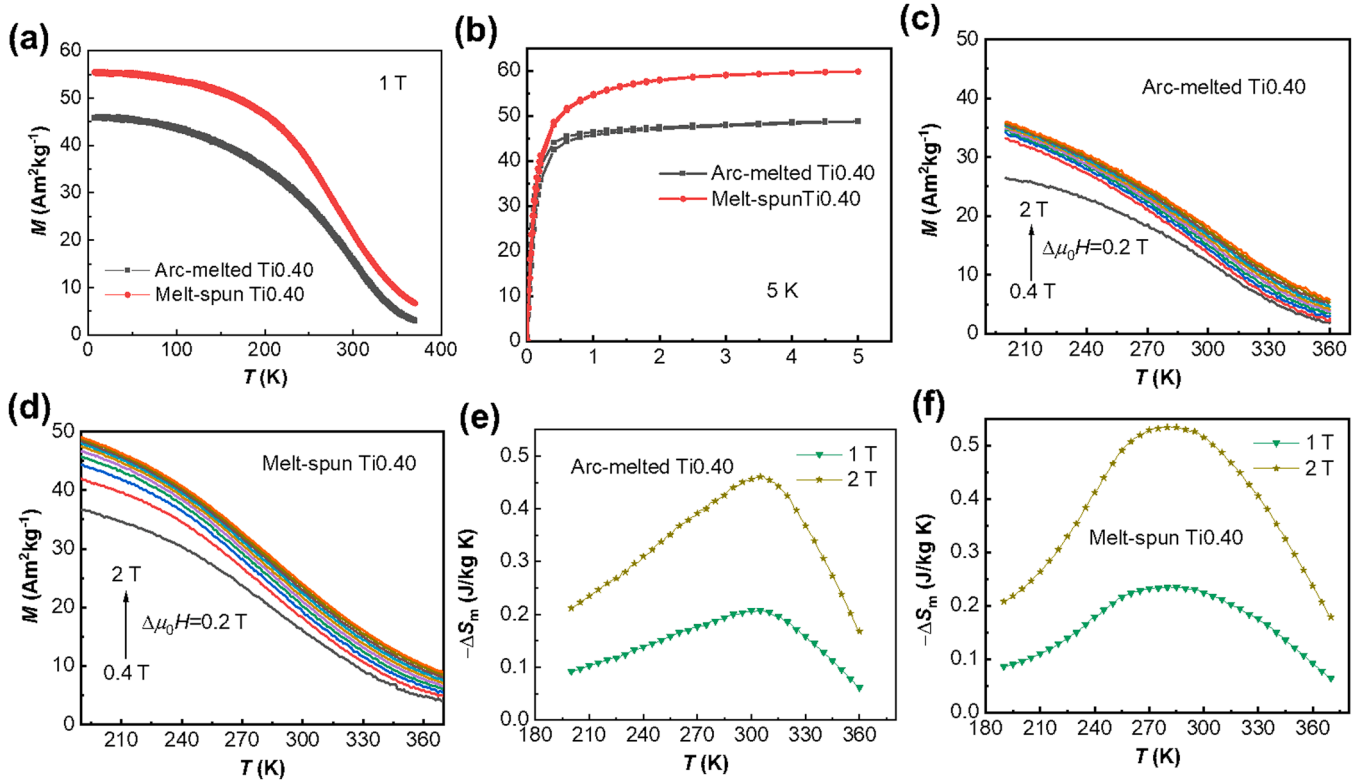

Fig. 5. (a) *M-T* curves of arc-melted and melt-spun Ti0.40 samples in a magnetic field of 1 T. (b) *M-H* curves of arc-melted and melt-spun Ti0.40 samples at 5 K. *M-T* curves upon heating in different applied magnetic fields for (c) arc-melted Ti0.40 and (d) melt-spun Ti0.40 samples. Magnetic entropy change $-\Delta S_m$ calculated from the heating curves for (e) arc-melted Ti0.40 and for (f) melt-spun Ti0.40 samples.

phase materials such as Fe_2(Hf,Nb) [27,40], where the cause of phase segregation is attributed to the positive mixing energy calculated by DFT. However, this is ruled out for Fe_2(Hf,Ti), since the formation energy for both the AFM and FM state is about −9 eV according to the DFT calculation in Fig. 3(g). For Fe_2(Hf,Ti), the large difference in atom size (7.5%) between Hf (159 pm) and Ti (147 pm) could be responsible for the phase segregation in high-Ti content samples, since a similar phase segregation was observed in the perovskite oxides $Gd_{1-x}Sr_xFeO_{3-\delta}$ [43], which was caused by the large size mismatch of 10% for Gd and Sr ions. Phase segregation is a way to relieve local stresses due to a size mismatch.

As a rapid solidification technology, melt-spinning process is found to suppress phase segregation in $Fe_2Hf_{1-x}Ti_x$ samples with a high-Ti content (x = 0.30, 0.33, 0.36, 0.40). Fig. 4(a) shows the homogeneous microstructure for the melt-spun Ti0.36 sample on the wheel side prepared with a wheel surface speed of 17 m/s. For melt-spun ribbons, the free side of the ribbon has a lower cooling rate than the wheel side of the ribbon [44]. Therefore, for the Ti0.36 (17 m/s) sample on the free side, the Ti-rich phase can be seen at the grain boundaries, while it is not observed in Ti0.36 (22 m/s) sample. From Fig. 4(b-c) the ribbons are found to be well crystalline with a grain size of about 1–3 μm. Line scanning across the grain boundaries shows that the Ti0.36 (22 m/s) sample is more homogeneous than the Ti0.36 (17 m/s) sample and thus the magnetic transition is sharper than the latter (see Fig. S5(a) in Supplementary Material). Compared to the arc-melting technique, the improved homogeneity in melt-spun samples can be attributed to the fact that the high solidification rate of the melt-spinning process suppresses phase segregation. Therefore, a wheel speed of 30 m/s is used for the melt-spun Ti0.40 sample.

The XRD pattern of the melt-spun Ti0.40 (30 m/s) sample shows a single hexagonal $MgZn_2$-type phase (see Fig. S6 in Supplementary Material). Fig. 5(a) and 5(b) show the *M-T* and *M-H* curves for the arc-melted and melt-spun Ti0.40 samples. The T_C (283 K) of the melt-spun Ti0.40 sample is lower than that of the arc-melted sample (309 K). This can be explained by the fact that the Ti in the melt-spun sample is more homogeneously distributed than in the arc-melted sample, so in the latter only part of the Ti plays a role in reducing T_C. The increased amount of ferromagnetic contribution at high temperature in melt-spun sample can be ascribed to the anti-site disorder of Fe atoms introduced by the melt-spinning process, which is also observed in $(La,Ce)(Fe,Si)_{13}$ [44] and melt-spun Fe_2(Hf,Ta) [45]. On the other hand, M_s increases by 22% from 48.7 Am^2/kg in the arc-melted sample to 59.6 Am^2/kg in the melt-spun sample due to the more homogeneous microstructure. The magnetic entropy change ΔS_m shown in Fig. 5(e) and 5(f) is calculated from the isofield magnetization curves in Fig. 5(c) and 5(d) using the Maxwell relation: $\Delta S_m(\Delta H,\ T) = \int_{H_0}^{H} \left(\frac{\partial M(T,H)}{\partial T}\right)_H \mathrm{d}\mu_0 H$, where we choose $\mu_0 H_0$ = 0 T. For the arc-melted Ti0.40 sample, $|\Delta S_m|$ broadens asymmetrically towards the low-temperature region as the magnetic field is increased, whereas the shape of $|\Delta S_m|$ becomes symmetric for the melt-spun sample. The magnetic entropy change $|\Delta S_m|$ under a magnetic field change of 2 T for arc-melted and melt-spun Ti0.40 sample is 0.46 J/kgK at 306 K and 0.54 J/kg K at 280 K, respectively. The melt-spun Ti0.40 sample generates a 20% higher magnetic entropy change. The value of $|\Delta S_m|$ for arc-melted Ti0.15 and Ti0.27 samples is calculated to be 1.1 and 1.0 J/kgK, respectively (see Fig. S7(b) and Fig. S7(e) in Supplementary Material). The Arrott-plots of the arc-melted Ti0.15 and Ti0.27 samples in Fig. S7(c) and S7(f) (Supplementary Material) prove that the phase transitions are of second-order, which is consistent with the broad exothermic and endothermic peaks in the DSC curves (see Fig. S8 in Supplementary Material). The $|\Delta S_m|$ of $Fe_2Hf_{1-x}Ti_x$ for a magnetic field change of 2 T is comparable to other Fe-based Laves phase materials with a SOMT, with 0.4 J/kgK in $Sc_{0.35}Ti_{0.65}Fe_{1.95}$ [46], but it is smaller than Fe-based Laves phase materials with a FOMT, with 1.4 J/kgK in $Sc_{0.35}Ti_{0.65}Fe_{1.95}$ [46] and 2.3 J/kgK in $Fe_2Hf_{0.86}Ta_{0.14}$ [13].

To analyse the nature of the magnetoelastic transition in this system, powder neutron diffraction (ND) and Mössbauer spectroscopy were used to study the single-phase arc-melted Ti0.15 sample. To eliminate possible strains due to thermal gradients during arc-melting, the sample was quenched into water after annealing at 1273 K for 32 h. A detailed Rietveld analysis was performed to refine the crystal structure and magnetic structure from the neutron diffraction patterns at different temperatures. The diffraction patterns recorded at 573 K (PM phase) and 4 K (FM phase) are shown in Fig. 6(a) and 6(b). The diffraction pattern measured at 573 K is characteristic for the nuclear Bragg scattering (PM phase) and was fitted to the $MgZn_2$-type phase with $P6_3/mmc$ symmetry. The ND pattern obtained at 4 K shows no additional reflections compared to the paramagnetic diffraction pattern. The analysis of the magnetic reflections indicates that the corresponding magnetic structure is defined by the propagation vector $\boldsymbol{k}$ = (0,0,0), which means that the magnetic unit cell coincides with the crystallographic one [13]. The arc-melted Ti0.15 sample shows a ferromagnetic ordering of Fe moments below 400 K, which is in good agreement with the T_C (392 K) from SQUID measurements. The FM ordering only increases the intensity at the nuclear peaks. The magnetic contributions are most pronounced at the (100), (101) and (002) peaks. The magnetic Fe moments were independently refined for the two sites. The best fit corresponds to magnetic moments that lie within the basal plane of the hexagonal lattice. The corresponding FM spin configuration is shown in Fig. 6(c). A summary of the crystallographic parameters and the refined Fe moments at different temperatures is shown in Table 1. The total moment of 3.14 μ_B/f.u. (calculated by $3/2\,M_{Fe(6h)} + 1/2\,M_{Fe(2a)}$) obtained from ND at 4 K agrees well with the 3.19 μ_B/f.u. calculated by DFT.

The temperature dependence of the lattice constants a and c, and the unit-cell volume V are displayed in Fig. 6(d,e). The lattice constant c increases continuously, while a only increases slowly from 4 to 300 K and, then decreases from 300 to 400 K and finally increases again from 400 to 573 K. As a result, V decreases abnormally from 300 to 400 K. The drop in lattice constant a is about 0.15%, about half that of $Hf_{0.86}Ta_{0.14}Fe_2$ [13]. The unit-cell volume of the FM phase is larger than that of the PM phase, and the spontaneous volume magnetostriction accompanying the second-order magnetic phase transition is estimated to be about $\Delta V/V$ = 0.25%. The negative thermal expansion observed from 300 K (171.63 Å^3) to 400 K (171.20 Å^3) leads to a negative thermal expansion coefficient $\alpha_v = (1/V)(\Delta V/\Delta T) = -25 \times 10^{-6}\ K^{-1}$ over a temperature range of 100 K, in agreement with [26]. This negative thermal expansion coefficient is comparable to commercial NTE materials like ZrW_2O_8 (α_v= −27.3 × 10^{-6} K^{-1}, 0–300 K) [47] and $PbTiO_3$ (α_v = −19.9 × 10^{-6} K^{-1}, 298–763 K) [48] and other Fe-based Laves phase materials like $Hf_{0.80}Nb_{0.20}Fe_2$ (α_v = −15 × 10^{-6} K^{-1}, 150–240 K) [27], and $Hf_{0.80}Ta_{0.20}Fe_2$ (α_v = −57.6 × 10^{-6} K^{-1}, 250–340 K) [20].

The Mössbauer spectra of arc-melted Ti0.15 and melt-spun Ti0.40 samples are shown in Fig. 7(a-f). The area ratio of the components corresponding to the Fe(6*h*) and Fe(2*a*) sites was set to 3:1 [40,49]. Table 2 summarizes the fitted parameters for the Mössbauer spectra at different temperatures. The small linewidth (0.4 mm/s) for all sites (except for the relaxing phase) indicates a good quality of fit for the spectra. The similar isomer shift and quadrupole splitting for Fe at the 2*a* and 6*h* sites indicates that both sites have a similar electronic state [50]. For the arc-melted Ti0.15 sample, the spectrum exhibits a paramagnetic feature at 400 K, which is consistent with the neutron diffraction results. The spectra at 4.2, 120 and 300 K contain two magnetic sub-spectra, attributed to the Fe(6*h*) and Fe(2*a*) sites. The hyperfine fields for the Ti0.15 sample at 4 K are 19.6 T and 17.2 T at the 6*h* and 2*a* sites, respectively. Using a proportionality factor of 14.2 T/μ_B [51] yields magnetic moments for the Fe(6*h*) site and the Fe(2*a*) site of 1.4 μ_B and 1.2 μ_B, respectively. This is in reasonable agreement with the ND results (see Table 1). At 350 K, the spectrum consists of a sextet magnetic sub-spectrum and a quadrupole doublet, which is considered to be the

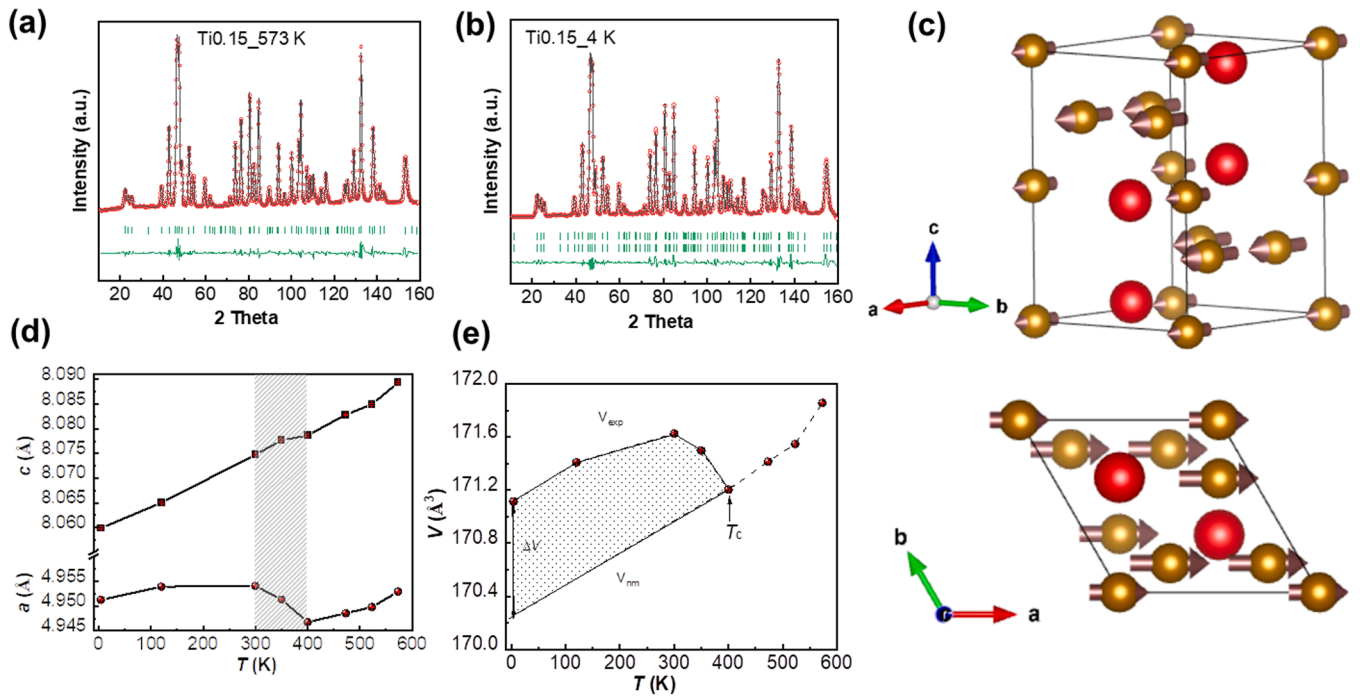

Fig. 6. Powder neutron diffraction (ND) patterns for the arc-melted Ti0.15 sample (a) at 573 K and (b) at 4 K. The top row of marked Bragg peak positions is from the nuclear contribution. The second row in (b) corresponds to the magnetic contribution. (c) Refined magnetic moment configuration. Temperature dependence of refined parameters: (d) lattice constants a and c and (e) experimental and non-magnetic unit-cell volume (V_{exp} and V_{nm}) from ND as a function of temperature for the arc-melted Ti0.15 sample. V_{nm} is calculated by the extrapolation of the high temperature data for the non-magnetic PM phase by ignoring the expected low-temperature levelling of the thermal expansion. The hatched zone in (d) indicates the NTE window.

Table 1
Fitted neutron diffraction parameters of the Ti0.15 sample obtained at different temperatures. The lattice structure corresponds to the $P6_3/mmc$ symmetry (space group 194) with the Fe atoms at the 2*a* site with position (0, 0, 0) and the 6*h* site with position (x, 2x, 1/4) and the Hf/Ti atoms at the 4*f* site with position (1/3, 2/3, z).

T (K)	*Phase*	$x_{(6h)}$	$z_{(4f)}$	c/a	M_{Fe} (6h) (μ_B/f. u.)	M_{Fe} (2a) (μ_B/f. u.)	χ^2
573	PM	0.16932 (19)	0.56275 (15)	1.62801 (4)	-	-	11.0
523	PM	0.16930 (19)	0.56309 (15)	1.63339 (3)	-	-	13.9
473	PM	0.16933 (19)	0.56277 (15)	1.62992 (4)	-		11.9
400	PM	0.16933 (22)	0.56258 (18)	1.63312 (3)	-	-	21.5
350	FM	0.16886 (23)	0.56285 (18)	1.63142 (4)	0.70	0.73	25.3
300	FM	0.16907 (19)	0.56230 (15)	1.63338 (3)	1.16	1.38	13.6
120	FM	0.16894 (16)	0.56253 (13)	1.63326 (3)	1.20	1.58	21.1
4	FM	0.16890 (16)	0.56236 (16)	1.62785 (4)	1.39	1.61	18.3

relaxing phase, with a coexistence of the ferromagnetic and the paramagnetic phase (45%) [52]. This coexistence of FM and PM phases is consistent with the ND data at 350 K.

The temperature dependence of the hyperfine field at the 2*a* and 6*h* sites is shown in Fig. 8(a). It is clear that the compound exhibits a ferromagnetic-to-paramagnetic transition between 350 and 400 K, which is consistent with the neutron diffraction results in Fig. 8(b). The magnetic hyperfine fields of Fe atoms at the 2*a* and 6*h* sites decrease simultaneously with increasing temperature, which is different from $Fe_2Hf_{0.8}Ta_{0.2}$ [49] and $Fe_2Hf_{0.9}Nb_{0.1}$ [40]. For $Hf_{0.8}Ta_{0.2}Fe_2$, the hyperfine field of Fe at the 2*a* site decreases to zero at the critical temperature of the first-order FM-AFM transition and the hyperfine field of Fe at the 6*h* site decreases to zero at the Curie temperature. The wide NTE window for (Hf,Ta)Fe_2 is attributed to the asynchronous FM ordering of Fe moments at 6*h* and 2*a* sites revealed by electron spin resonance [20]. As in the case in Fe_2(Hf,Ti), the simultaneous decrease of the hyperfine field of Fe at the 2*a* and 6*h* sites indicates a second-order transition. Fig. 8(c) and 8(d) show the interatomic distances of Fe atoms derived from ND. The interlayer spacing of Fe_{6h}-Fe_{6h}, Fe_{6h}-Fe_{2a} and Fe_{6h}-Hf/Ti_{4f} increases linearly with increasing temperature, while a sharp decrease of 0.36% in the intralayer spacing of Fe_{6h}-Fe_{6h} is observed within the NTE temperature range. This phenomenon could originate from the fact that the shortest Fe_{6h}-Fe_{6h} distance controls the magnetic interactions in Fe_2(Hf,Ti). A similar trend is also reported for the temperature dependence of magnetism in $Sc_{0.4}Ti_{0.6}Fe_2$ [21] and the pressure-dependant magnetism in $Mn_3Ga_{0.95}N_{0.94}$ [53].

To reveal the relation between negative thermal expansion and the magnetic order, the spontaneous volume magnetostriction is calculated by subtracting the thermal expansion of the nonmagnetic phase from the experimental one. The magnitude of the spontaneous volume magnetostriction can be defined as $\omega_s = \frac{V_{exp}-V_{nm}}{V_{nm}} \times 100\%$, where V_{exp} and V_{nm} (shown in Fig. 6(e)) are the unit-cell volumes of experimental and the non-magnetic phases, respectively [21,54]. Fig. 8(e) shows $d\omega_s/dT$ and dM/dT as a function of temperature. Both $d\omega_s/dT$ and dM/dT show the same trend, indicating a strong coupling between magnetism and lattice in this system. A sharp magnetic transition indicates a strong contribution of the spontaneous magnetostriction to the thermal contraction, which contributes to the occurrence of the NTE, as also reported in Mn_3Ge [55] and $Fe_2Zr_{0.7}Nb_{0.3}$ [56]. Based on the ND results, the shortest in-plane Fe_{6h}-Fe_{6h} distance controls the magnetic interactions of Fe_2(Hf, Ti), so the rate at which the in-plane Fe magnetic moments decrease with temperature governs the negative thermal expansion.

A linear correlation between the square of the Fe magnetic moment

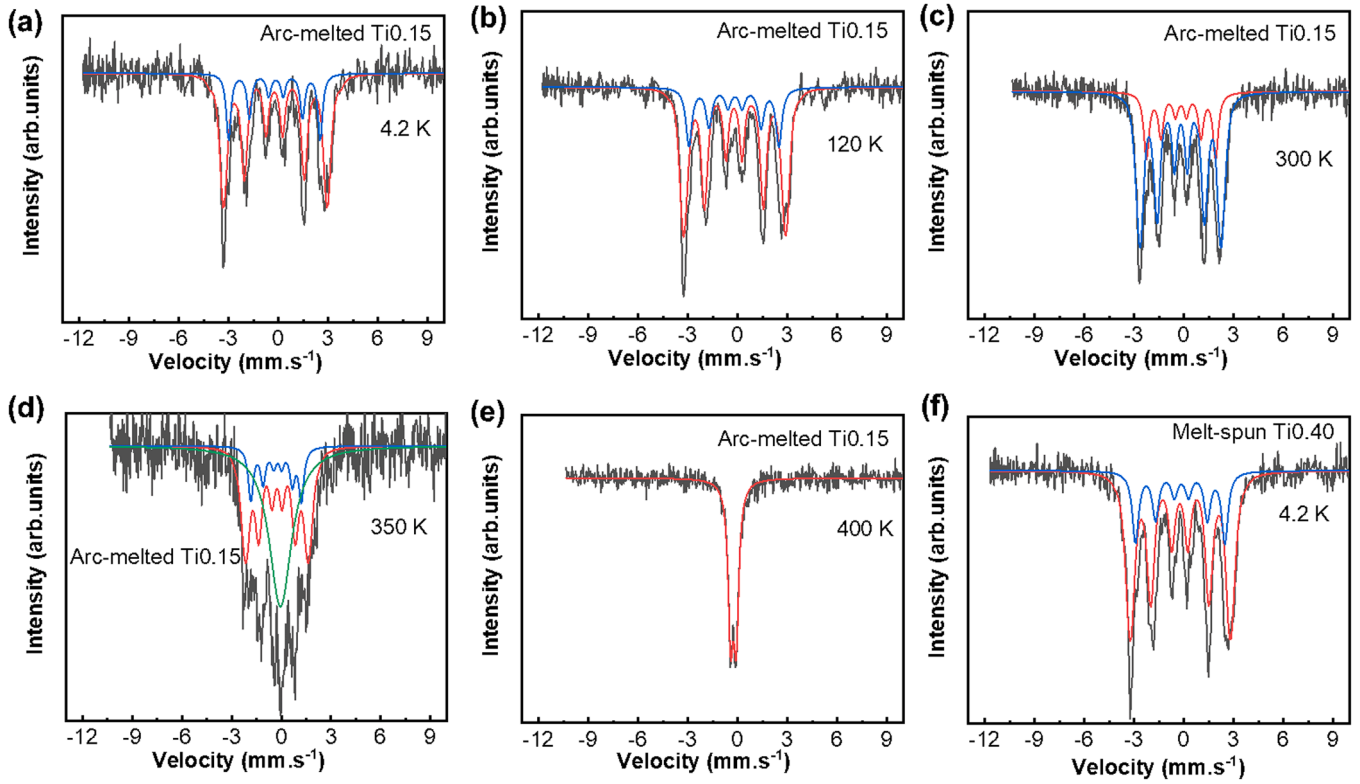

Fig. 7. Mössbauer spectra of the arc-melted Ti0.15 sample at (a) 4.2 K, (b) 120 K, (c) 300 K, (d) 350 K, (e) 400 K. (f) Mössbauer spectra of the melt-spun Ti0.40 sample at 4.2 K. The black line represents the experimental spectrum.

Table 2
Fitted Mössbauer parameters of the selected (Hf,Ti)Fe_2 samples, obtained at different temperatures. Experimental uncertainties: Isomer shift: I.S. ± 0.03 mm s^{-1}; Quadrupole splitting: Q.S. ± 0.03 mm s^{-1}; Line width: Γ ± 0.05 mm s^{-1}; Hyperfine field: ± 0.2 T; Spectral contribution: ± 3%. FM: ferromagnetic phase; PM: paramagnetic phase.

Sample	Temperature (K)	IS (mm s^{-1})	QS (mm s^{-1})	Hyperfine field (T)	Γ (mm s^{-1})	Phase
Melt-spun Ti0.40	4.2 K	−0.23	0.03	18.9	0.46	FM (6*h*)
		−0.19	−0.08	16.7	0.46	FM (2*a*)
Arc-melted Ti0.15	4.2 K	−0.21	0.06	19.6	0.38	FM (6*h*)
		−0.19	−0.09	17.2	0.33	FM (2*a*)
	120 K	−0.20	0.04	19.1	0.36	FM (6*h*)
		−0.19	−0.07	16.9	0.43	FM (2*a*)
	300 K	−0.21	−0.01	15.3	0.41	FM (6*h*)
		−0.19	−0.04	13.1	0.43	FM (2*a*)
	350 K	−0.27	−0.01	12.0	0.43	FM (6*h*)
		−0.27	−0.09	9.5	0.38	FM (2*a*)
		−0.05	-	-	1.65	PM
	400 K	−0.26	0.34	-	0.37	PM

and ω_s is found in Fig. 8(f). The magnetic-lattice coupling can quantitatively be described by: $\omega_s(T) = kCM(T)^2$ [57], where k and C are the compressibility and the magneto-volume coupling constant, and M is the magnetic moment. The constant kC for the $Fe_2Hf_{0.85}Ti_{0.15}$ sample can be obtained from the slope of the curve in Fig. 8(f). For $Fe_2Hf_{0.85}Ti_{0.15}$, the constant kC at 4.2 K is calculated to be 1.48×10^{-10} cm^2/A^2. This value is of the same order of magnitude as those for $Fe_2Hf_{0.83}Ta_{0.17}$ (1.32×10^{-10} cm^2/A^2) [41] and $La(Fe_{0.86}Al_{0.24})_{13}$ (1.79×10^{-10} cm^2/A^2) [58], which are potential MCE materials with a strong magnetoelastic coupling. Short-range disorder, either caused by phase segregation in the Fe_2(Hf,Ti) system ascribed to the large difference in Hf and Ti atoms sizes or due to rapid solidification, may account for the second-order phase transition in this magnetoelastic material.

4. Conclusions

In summary, we have studied the crystal structure, microstructure, and magnetic properties of arc-melted and melt-spun $Fe_2Hf_{1-x}Ti_x$ (x = 0.15, 0.27, 0.30, 0.33, 0.36, 0.40) alloys, which are derived from two isostructural $HfFe_2$ and $TiFe_2$ Laves phase materials. Surprisingly, a phase segregation is found in samples with x = 0.30–0.40, which we attribute to the 7.5% size difference between Hf and Ti. The high cooling rate achieved by melt-spinning at a wheel speed of 30 m/s yields homogeneous alloys. The magnetic transition temperature decreases linearly with the average unit-cell volume. The saturation magnetization suppressed by phase segregation can be recovered from 48.7 Am^2/kg to 59.6 Am^2/kg by melt spinning and thus the magnetocaloric effect can be enhanced from 0.46 to 0.54 J/kg K under a magnetic field change of 2 T due to the improved homogeneity. ND results reveal that the magnetic moments lie within the *a*-*b* plane, and the reduction in magnetic moment

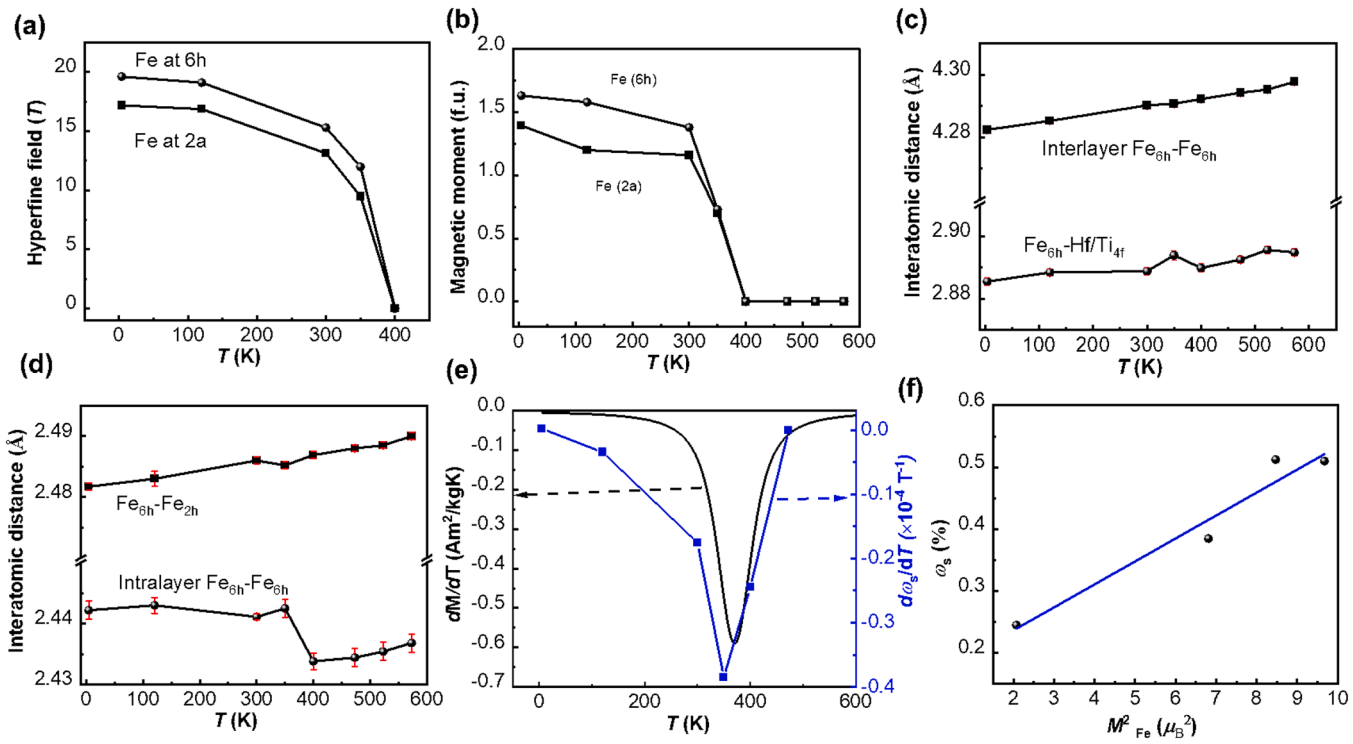

Fig. 8. (a) Temperature dependence of the hyperfine field of the arc-melted Ti0.15 sample, derived from Mössbauer spectroscopy. (b) Temperature dependence of magnetic moment at the 2*a* and 6*h* site of the arc-melted Ti0.15 sample derived from ND (Table 1). (c-d) Interatomic distance as a function of temperature. (e) dω_s/dT and dM/dT (at a magnetic field of 1 T) as a function of temperature. (f) ω_s as a function of the square of the Fe magnetic moment.

of the Fe atoms is consistent with the abnormal decrease in the lattice parameter a with increasing temperature. We observe a negative thermal expansion ($-25 \times 10^{-6}\ K^{-1}$) for the single-phase $Fe_2Hf_{0.85}Ti_{0.15}$ compound over a wide temperature range of 300–400 K. The relation between the negative thermal expansion and the magnetism is discussed by quantitatively analysing the correlation between the spontaneous magnetostriction and magnetic moment of the Fe atoms. Our results provide a significant insight into the magnetoelastic coupling in these magnetocaloric materials and provide an experimental route to solve common fabrication problems in Fe-based Laves phase materials.

Declaration of Competing Interest

The authors declare that they have no known competing financial interests or personal relationships that could have appeared to influence the work reported in this paper.

Acknowledgements

This work is part of the project 'Energy conversion with highly responsive magnetic materials for efficiency' funded by the Dutch Research Council with Project no. 680-91-–013 and co-financed by Swiss Blue Energy and RSP Technology. The authors thank Anton Lefering, Bert Zwart, Robert Dankelman and Michel Steenvoorden for their technical assistance.

Supplementary materials

Supplementary material associated with this article can be found, in the online version, at doi:10.1016/j.actamat.2023.119149.

References

[1] O. Tegus, E. Brück, K.H.J. Buschow, F.R. de Boer, Transition-metal-based magnetic refrigerants for room-temperature applications, Nature 415 (2002) 150–151.
[2] X. Moya, S. Kar-Narayan, N.D. Mathur, Caloric materials near ferroic phase transitions, Nat. Mater. 13 (2014) 439–450.
[3] E. Brück, Developments in magnetocaloric refrigeration, J. Phys. D: Appl. Phys. 38 (2005) R381–R391.
[4] K.G. Sandeman, Magnetocaloric materials: the search for new systems, Scr. Mater. 67 (2012) 566–571.
[5] N.H. Dung, Z.Q. Ou, L. Caron, L. Zhang, D.T.C. Thanh, G.A. de Wijs, R.A. de Groot, K.H.J. Buschow, E. Brück, Mixed magnetism for refrigeration and energy conversion, Adv. Energy Mater. 1 (2011) 1215–1219.
[6] F. Guillou, G. Porcari, H. Yibole, N. van Dijk, E. Bruck, Taming the first-order transition in giant magnetocaloric materials, Adv. Mater. 26 (2014) 2671–2675.
[7] F. Hu, B. Shen, J. Sun, Z. Cheng, G. Rao, X. Zhang, Influence of negative lattice expansion and metamagnetic transition on magnetic entropy change in the compound $LaFe_{11.4}Si_{1.6}$, Appl. Phys. Lett. 78 (2001) 3675–3677.
[8] J. Liu, J.D. Moore, K.P. Skokov, M. Krautz, K. Löwe, A. Barcza, M. Katter, O. Gutfleisch, Exploring $La(Fe,Si)_{13}$-based magnetic refrigerants towards application, Scr. Mater. 67 (2012) 584–589.
[9] J. Liu, T. Gottschall, K.P. Skokov, J.D. Moore, O. Gutfleisch, Giant magnetocaloric effect driven by structural transitions, Nat. Mater. 11 (2012) 620–626.
[10] T. Krenke, M. Acet, E.F. Wassermann, X. Moya, L. Mañosa, A. Planes, Martensitic transitions and the nature of ferromagnetism in the austenitic and martensitic states of Ni-Mn-Sn alloys, Phys. Rev. B 72 (2005), 014412.
[11] N.T. Trung, L. Zhang, L. Caron, K.H.J. Buschow, E. Brück, Giant magnetocaloric effects by tailoring the phase transitions, Appl. Phys. Lett. 96 (2010), 172504.
[12] L.V.B. Diop, J. Kastil, O. Isnard, Z. Arnold, J. Kamarad, Magnetic and magnetocaloric properties of itinerant-electron system $Hf_{1-x}Ta_xFe_2$ ($x = 0.125$ and 0.175), J. Alloys Compd. 627 (2015) 446–450.
[13] L.V.B. Diop, O. Isnard, M. Amara, F. Gay, J.P. Itié, Giant negative thermal expansion across the first-order magnetoelastic transition in $Hf_{0.86}Ta_{0.14}Fe_2$, J. Alloys Compd. 845 (2020), 156310.
[14] Z. Song, Z. Li, B. Yang, H. Yan, C. Esling, X. Zhao, L. Zuo, Large low-field reversible magnetocaloric effect in itinerant-electron $Hf_{1-x}Ta_xFe_2$ alloys, Materials (Basel) 14 (2021) 1–11.
[15] L. Caron, X.F. Miao, J.C.P. Klaasse, S. Gama, E. Brück, Tuning the giant inverse magnetocaloric effect in $Mn_{2-x}Cr_xSb$ compounds, Appl. Phys. Lett. 103 (2013), 112404.
[16] Z. Zhang, Y. Zhang, X. Luo, S. Ma, H. Zeng, G. Yu, X. Zheng, C. Chen, Y. Hu, F. Xu, S.U. Rehman, Z. Zhong, Self-organized Bi-rich grain boundary precipitates for realizing steep magnetic-field-driven metamagnetic transition in Bi-doped Mn_2Sb, Acta Mater 200 (2020) 835–847.
[17] Q. Shen, I. Batashev, F. Zhang, H. Ojiyed, N. van Dijk, E. Brück, The antiferromagnetic to ferrimagnetic phase transition in $Mn_2Sb_{1-x}Bi_x$ compounds, J. Alloys Compd. 866 (2021).

[18] R. Huang, Y. Liu, W. Fan, J. Tan, F. Xiao, L. Qian, L. Li, Giant negative thermal expansion in $NaZn_{13}$-type La(Fe,Si,Co)$_{13}$ compounds, J Am. Chem. Soc. 135 (2013) 11469–11472.

[19] Y.Y. Zhao, F.X. Hu, L.F. Bao, J. Wang, H. Wu, Q.Z. Huang, R.R. Wu, Y. Liu, F. R. Shen, H. Kuang, M. Zhang, W.L. Zuo, X.Q. Zheng, J.R. Sun, B.G. Shen, Giant negative thermal expansion in bonded MnCoGe-based compounds with Ni_2In-type hexagonal structure, J. Am. Chem. Soc. 137 (2015) 1746–1749.

[20] L.F. Li, P. Tong, Y.M. Zou, W. Tong, W.B. Jiang, Y. Jiang, X.K. Zhang, J.C. Lin, M. Wang, C. Yang, X.B. Zhu, W.H. Song, Y.P. Sun, $Hf_{1-x}TaxFe_2$ as negative thermal expansion materials, Acta Mater 161 (2018) 258–265.

[21] Y. Song, Q. Sun, M. Xu, J. Zhang, Y. Hao, Y. Qiao, S. Zhang, Q. Huang, X. Xing, J. Chen, Negative thermal expansion in (*Sc*,Ti)Fe_2 induced by an unconventional magnetovolume effect, Mater. Horiz. 7 (2020) 275–281.

[22] F. Hu, F. Shen, J. Hao, Y. Liu, J. Wang, J. Sun, B. Shen, Negative thermal expansion in the materials with giant magnetocaloric effect, Front Chem 6 (2018) 438.

[23] Y. Song, N. Shi, S. Deng, X. Xing, J. Chen, Negative thermal expansion in magnetic materials, Prog. Mater. Sci. 121 (2021) 11835.

[24] B. Li, X.H. Luo, H. Wang, W.J. Ren, S. Yano, C.W. Wang, J.S. Gardner, K.D. Liss, P. Miao, S.H. Lee, T. Kamiyama, R.Q. Wu, Y. Kawakita, Z.D. Zhang, Colossal negative thermal expansion induced by magnetic phase competition on frustrated lattices in Laves phase compound (Hf,Ta)Fe_2, Phys. Rev. B 93 (2016), 224405.

[25] H.R. Rechenberg, L. Morellon, P.A. Algarabel, M.R. Ibarra, Magnetic moment at highly frustrated sites of antiferromagnetic Laves phase structures, Phys. Rev. B 71 (2005), 104412.

[26] Y. Qiao, Y. Song, K. Lin, X. Liu, A. Franz, Y. Ren, J. Deng, R. Huang, L. Li, J. Chen, X. Xing, Negative thermal expansion in (Hf,Ti)Fe_2 induced by the ferromagnetic and antiferromagnetic phase coexistence, Inorg. Chem. 58 (2019) 5380–5383.

[27] H. Yibole, A.K. Pathak, Y. Mudryk, F. Guillou, N. Zarkevich, S. Gupta, V. Balema, V. K. Pecharsky, Manipulating the stability of crystallographic and magnetic sub-lattices: a first-order magnetoelastic transformation in transition metal based Laves phase, Acta Mater. 154 (2018) 365–374.

[28] B.H. Toby, R factors in Rietveld analysis: how good is good enough? Powder Diffr. 21 (2012) 67–70.

[29] Z. Klencsar, Mossbauer spectrum analysis by evolution algorithm, Nucl. Instr. Meth. Phys. Res. B 129 (1997) 527–533.

[30] L. van Eijck, L.D. Cussen, G.J. Sykora, E.M. Schooneveld, N.J. Rhodes, A.A. van Well, C. Pappas, Design and performance of a novel neutron powder diffractometer: PEARL at TU Delft, J. Appl. Crystallogr. 49 (2016) 1398–1401.

[31] H.M. Rietveld, Line profiles of neutron powder-diffraction peaks for structure refinement, Acta cryst 22 (1967) 151–152.

[32] T.M. Sabine, Powder neutron diffraction-refinement of the total pattern, J. Appl. Cryst. 10 (1977) 277–280.

[33] J. Rodriguez-Carvajal, Recent advances in magnetic structure determination by neutron powder diffraction, Physica B 192 (1993) 55–69.

[34] G. Kresse, J. Hafner, Ab initio molecular dynamics for liquid metals, Phys. Rev. B Condens Matter 47 (1993) 558–561.

[35] G. Kresse, J. Furthmiiller, Efficiency of ab-initio total energy calculations for metals and semiconductors using a plane-wave basis set, Comput. Mater. Sci. 6 (1996) 15–50.

[36] J.P. Perdew, K. Burke, M. Ernzerhof, Generalized gradient approximation made simple, Phys. Rev. Lett. 77 (1996) 3865–3868.

[37] P.E. Blochl, Projector augmented-wave method, Phys. Rev. B: Condens Matter 50 (1994) 17953–17979.

[38] G. Kresse, D. Joubert, From ultrasoft pseudopotentials to the projector augmented-wave method, Phys. Rev. B 59 (1999) 1758–1775.

[39] M. Methfessel, A.T. Paxton, High-precision sampling for Brillouin-zone integration in metals, Phys. Rev. B: Condens Matter 40 (1989) 3616–3621.

[40] Y. Song, J. Chen, X. Liu, C. Wang, Q. Gao, Q. Li, L. Hu, J. Zhang, S. Zhang, X. Xing, Structure, magnetism, and tunable negative thermal expansion in (Hf,Nb)Fe_2 alloys, Chem. Mater. 29 (2017) 7078–7082.

[41] Y. Huang, Z. Han, Z. Jiang, S. Li, Y. Hsia, Microscopic magnetic properties of itinerant-electron system $Hf_{0.8}Ta_{0.2}(Fe_{1-x}Co_x)_2$ (x = 0-0.09): a Mössbauer study, Physica B: Condensed Matter 388 (2007) 354–358.

[42] M. Saoudia, J. Deportes, B. Ouladdiaf, Magnetic ground state of $Ti_{1-x}Sc_xFe_2$ system, J. Magn. Magn. Mater. 231 (2001) 265–272.

[43] J. Blasco, J. Stankiewicz, J. García, Phase segregation in the $Gd_{1-x}SrxFeO_{3-\delta}$ series, J. Solid State Chem. 179 (2006) 898–908.

[44] J. Yang, Y. Shao, Z. Feng, J. Liu, The effect of cooling rate on the phase formation and magnetocaloric properties in $La_{0.6}Ce_{0.4}Fe_{11.0}Si_{2.0}$ alloys, J. Magn. Magn. Mater. 452 (2018) 473–476.

[45] Q. Shen, F. Zhang, I. Dugulan, N. van Dijk, E. Brück, Magnetoelastic transition and negative thermal expansion of $Fe_2Hf_{0.83}Ta_{0.17}$ ribbons, Scr. Mater. 232 (2023).

[46] L. Sun, H. Yibole, O. Tegus, F. Guillou, $Sc_{0.28}Ti_{0.72}Fe_{2-x}T_x$ Alloys with T=Mn or Co, Crystals 10 (2020) 410.

[47] T.A. Mary, J.S.O. Evans, A.W.Sleight T.Vogt, Negative thermal expansion from 0.3 to 1050 Kelvin in ZrW_2O_8, Science 272 (1996) 92–94.

[48] J. Chen, X. Xing, R. Yu, G. Liu, Thermal expansion properties of lanthanum-substituted lead titanate ceramics, J. Am. Ceram. Soc. 88 (2005) 1356–1358.

[49] N.N. Delyagin, A.L. Erzinkyan, V.P. Parfenova, I.N. Rozantsev, G.K. Ryasny, Ferromagnetic-to-antiferromagnetic transition in $(Hf_{1-x}Ti_x)Fe_2$ intermetallic compounds induced by geometrical frustration of the Fe(2*a*) sites, J. Magn. Magn. Mater. 320 (2008) 1853–1857.

[50] Y.J. Huang, S.Z. Li, Z.D. Han, W.X. Wang, Z.Y. Jiang, S.L. Huang, J. Lin, Y.F. Hsia, Mössbauer study of the spin reorientation in pseudobinary alloy $Hf_{0.82}Ta_{0.18}Fe_2$, J. Alloys Compd. 427 (2007) 37–41.

[51] O. Eriksson, A. Svane, Isomer shifts and hyperfine fields in iron compounds, J. Phys.: Condens. Matter l (1989) 1589–1599.

[52] D. Huang, T. Ma, D.E. Brown, S.H. Lapidus, Y. Ren, J. Gao, Nanoscale phase separation and large refrigerant capacity in magnetocaloric material $LaFe_{11.5}Si_{1.5}$, Chem. Mater. 33 (2021) 2837–2846.

[53] K. Shi, Y. Sun, J. Yan, S. Deng, L. Wang, H. Wu, P. Hu, H. Lu, M.I. Malik, Q. Huang, C. Wang, Baromagnetic effect in antiperovskite $Mn_3Ga_{0.95}N_{0.94}$ by neutron powder diffraction analysis, Adv. Mater. 28 (2016) 3761–3767.

[54] Q. Li, K. Lin, Z. Liu, L. Hu, Y. Cao, J. Chen, X. Xing, Chemical diversity for tailoring negative thermal expansion, Chem. Rev. 122 (2022) 8438–8486.

[55] Y. Song, Y. Qiao, Q. Huang, C. Wang, X. Liu, Q. Li, J. Chen, X. Xing, Opposite thermal expansion in isostructural noncollinear antiferromagnetic compounds of Mn_3A (A = Ge and Sn), Chem. Mater. 30 (2018) 6236–6241.

[56] Y. Song, Q. Sun, T. Yokoyama, H. Zhu, Q. Li, R. Huang, Y. Ren, Q. Huang, X. Xing, J. Chen, Transforming thermal expansion from positive to negative: the case of cubic magnetic compounds of (Zr,Nb)Fe_2, J Phys. Chem. Lett. 11 (2020) 1954–1961.

[57] A. Fujita, K. Fukamichi, J.T. Wang, Y. Kawazoe, Large magnetovolume effects and band structure of itinerant-electron metamagnetic $La(Fe_xSi_{1-x})_{13}$ compounds, Phys. Rev. B 68 (2003).

[58] T.T. Palstra, G.J. Nieuwenhuys, J.A. Mydosh, K.H. Buschow, Mictomagnetic, ferromagnetic, and antiferromagnetic transitions in $La(Fe_xAl_{1-x})_{13}$ intermetallic compounds, Phys. Rev. B Condens. Matter. 31 (1985) 4622–4632.